Chemical Science

ROYAL SOCIETY OF CHEMISTRY

EDGE ARTICLE

View Article Online
View Journal | View Issue

Cite this: *Chem. Sci.*, 2026, **17**, 977

All publication charges for this article have been paid for by the Royal Society of Chemistry

Real-time tracking of molecular cluster assembly and precise hierarchical reassembly into pure POM host–guest architecture†

Kai-Ling Zhu,†[a] Ke Li,†[a] Liu-Bin Feng,[a] Le Yang[b] and Jia-Jia Chen *[a]

In this work, we report an *in operando* spectroscopy strategy to track the molecular cluster assembly and thereby realize a precise bottom-up hierarchical reassembly of building blocks into a pure POM host–guest architecture. Through precise flow chemical synthesis combined with *in operando* Raman characterization, we systematically tracked key building block intermediates emerging during the evolution from WO_4^{2-} precursors to the $\{P_2W_{18}\}$ cluster and validated with ESI-MS and ^{31}P NMR. Capitalizing on the dynamic assembly behaviour, we further realized precise hierarchical re-assembly of building blocks $PW_9O_{34}^{9-}$ ($\{PW_9\}$): eight $\{PW_9\}$ were used as secondary building units (SBUs) to form tertiary building units (TBUs, $K_{42}P_8W_{72}$, and $\{PW_9\}_8$), and then TBUs were further linked by alkali metals, resulting in a purely inorganic host–guest architecture $\{[K_{66}Na_{14}H_{10}(H_2O)_{150}(PW_9O_{34})_8]\cdot(PW_9O_{34})_2\cdot 43H_2O\}$ (compound **1**, $\{PW_9\}_2$@$\{PW_9\}_8$) with interpenetrating three-dimensional channels containing discrete nano-sized SBUs. Unlike the irreversible and limited electrochemical reaction behaviour of SBUs, compound **1** exhibited markedly distinct electrochemical properties with multi-step multi-electron redox behaviours at 0.23 V, 0.01 V, −0.49 V and −0.87 V *vs.* NHE, respectively. These findings refine the understanding of the assembly behaviours and pave the way for designing atomically defined and functional clusters.

Received 15th September 2025
Accepted 7th November 2025

DOI: 10.1039/d5sc07121f

rsc.li/chemical-science

Introduction

POMs are a class of polynuclear nanoclusters formed through a few to hundreds of transition metal atoms (*e.g.*, W, Mo, and V) linked by oxygen. They demonstrate profound fundamental research significance and application potential in cutting-edge fields including photoelectrocatalysis,[1–6] energy storage and conversion,[7–10] acid catalysis[11,12] and magnetic substances,[13,14] attributable to their unique topological structures that govern electronic configurations and spatial arrangements.[15–20]

Taking the representative Wells–Dawson POMs as an example, their structural characteristics involve polyhedral core units formed by central metal ions coordinated with oxygen atoms and these structural motifs further assemble into highly ordered three-dimensional spatial configurations through vertex-/edge-/plane-sharing. As an "electron sponge" with a unique structure, it demonstrated great potential in various fields. Specifically, $Li_6P_2W_{18}O_{62}$ demonstrated exceptional potential as high-capacity electroactive materials for redox flow batteries and hydrogen storage mediators through their reversible 18-electron/proton storage capability.[7] Heteroatom modification,[21] counterion exchange strategies,[8] or site-specific covalent functionalization[5] further modulate their physicochemical properties for specific applications, which exemplifies the remarkable structural tunability and functional potential of Dawson-type clusters. For instance, the selenite-containing Dawson-type cluster $[W_{18}O_{56}(SeO_3)_2(H_2O)_2]^{8-}$ exhibited a novel heteroatom oxidation state and has been employed as a nanoscale flash memory device, providing a strategy for integrating configurable molecules into a metal–oxide–semiconductor (MOS).[21] Streb *et al.* reported a ruthenium-complex photosensitizer covalently modified Dawson polyoxometalate, which further simultaneously possessed photosensitivity and electron-storage sites and was used as a mediator to achieve the spatially and temporally decoupled photocatalytic hydrogen evolution process.[5] Nevertheless, mechanistic understanding of solution-phase assembly of those clusters has lagged far behind the rapid progress in application studies.

Bottom-up synthesis has become an important methodology for the preparation of POMs. However, the intricate hierarchical assembly mechanisms remain poorly understood, akin to a "black box". Concurrently, advancements in characterization techniques have enabled multidimensional analysis of assembly mechanisms. Single-crystal X-ray diffraction (SCXRD)

[a]*State Key Laboratory for Physical Chemistry of Solid Surfaces, Innovation Laboratory for Sciences and Technologies of Energy Material of Fujian Province (IKKEM), Collaborative Innovation Center of Chemistry for Energy Materials (iChem), Engineering Research Center of Electrochemical Technologies of Ministry of Education, Department of Chemistry, College of Chemistry and Chemical Engineering, Xiamen University, Xiamen, Fujian 361005, China. E-mail: jiajia.chen@xmu.edu.cn*

[b]*College of Chemistry and Chemical Engineering, Southwest University, Chongqing 400715, China*

† K. Z. and K. L. contributed equally to this work.

provides atomic-level structural resolution through precise determination of crystallographic positions. Zheng *et al.* reported polyoxoniobates with molecular tweezers for selective transition metal capture. Ion exchange drove single-crystal-to-single-crystal transformation, with SCXRD unambiguously identifying the ion capture/release sites.[22] Neutron diffraction complements SCXRD in probing light elements and magnetic structures.[23] Electrospray ionization mass spectrometry (ESI-MS) monitors solution-phase assembly by identifying intermediates and measuring molecular weights.[24–26] Employing a geometric polyhedron strategy, Sun *et al.* presented a Goldberg polyhedral silver cage Ag_{180}. ESI-MS elucidated the assembly mechanisms of Ag_{180}, revealing the processes of "silver triangle" formation and "planar epitaxial growth".[24] Emerging characterization methodologies continue to expand our analytical capabilities for uncovering the assembly behaviours of building units in the solution phase. Addressing the synthetic challenges of the classical molybdenum-oxo cluster $\{Mo_{150}\}$, Leroy Cronin *et al.* innovated a dynamic flow reaction system that overcame the limitations of traditional static synthesis.[27] By precisely controlling the injection rate of $\{Mo_{36}\}$ building blocks and the reductant, they achieved accelerated formation of $\{Mo_{150}\}$, providing the experimental evidence of $\{Mo_{36}\}$ as critical templates in the molecular assembly process.

Hierarchical assembly provides a rational strategy for the structural design of POMs, enabling precise control over their spatial arrangement, electronic interactions, and resultant material properties. This approach further allows the construction of well-defined, purely inorganic POM-based host–guest architectures. Such systems serve as ideal platforms for elucidating intrinsic architectures and for guiding the development of advanced functional materials. However, the lack of *in situ* or *in operando* characterization for study of continuous and comprehensive assembly mechanisms has led to insufficient understanding of the precise reaction route in POM science, which further hindered controllable synthesis and rational design of atomically precise clusters.

Herein, we employed an integrated flow chemical synthesis-*in operando* spectral characterization system to monitor the solution-phase assembly process leading to the $\{P_2W_{18}\}$ cluster, aiming to track intermediate species and elucidate aspects of the reaction pathway. Key intermediate species ($\{PW_9\}$, $\{PW_{11}\}$, and $\{W_{12}\}$) in the solution assembly process were detected with support from ^{31}P nuclear magnetic resonance (NMR) and ESI-MS. Based on these mechanistic insights, we further propose an intermediate-directed reassembly strategy that successfully achieved hierarchical assembly with the using of $\{PW_9\}$ as the SBU through precise parameter control. The resulting compound **1** had a host–guest architecture with three-dimensional interpenetrating channels accommodating discrete $\{PW_9\}$, which exhibited intensified redox peaks with markedly enhanced redox activity compared to single $\{PW_9\}$. This work advanced fundamental understanding of POM self-assembly and further established a methodological guideline for the rational design of functionally oriented materials.

Results and discussion

Elucidating the evolutionary mechanisms from monomer precursors to complex hierarchical architectures holds dual scientific significance: (1) providing critical insights into the structure–property relationships at the nanoscale; (2) guiding the customized assembly of functional materials for practical applications. Tracking the reaction process in real time and elucidating the relationships between critical reaction parameters (*e.g.*, pH and temperature) and assembly pathways precisely remains challenging *via* conventional synthesis of polyoxometalates. Thus, we designed flow chemistry synthesis and combined it with *in operando* spectral characterization to visualize the assembly mechanism of Wells–Dawson $\{P_2W_{18}\}$. Distinct from conventional reactions involving instantaneous mixing of raw materials, the visualization device enabled precise regulation and real-time monitoring of reaction key intermediates.

The instrumental architecture (Fig. 1a) features two synergistic modules: a multichannel flow reaction module with controllable experimental operation parameters and a real-time analytical spectroscopy detection module. The reaction process comprised stage I, continuous infusion of H_3PO_4 (6.85 mL, flow rate 7.2 μL s^{-1}) for acidification and the provision of anion templates (PO_4^{3-}) in the assembly process. This was followed by

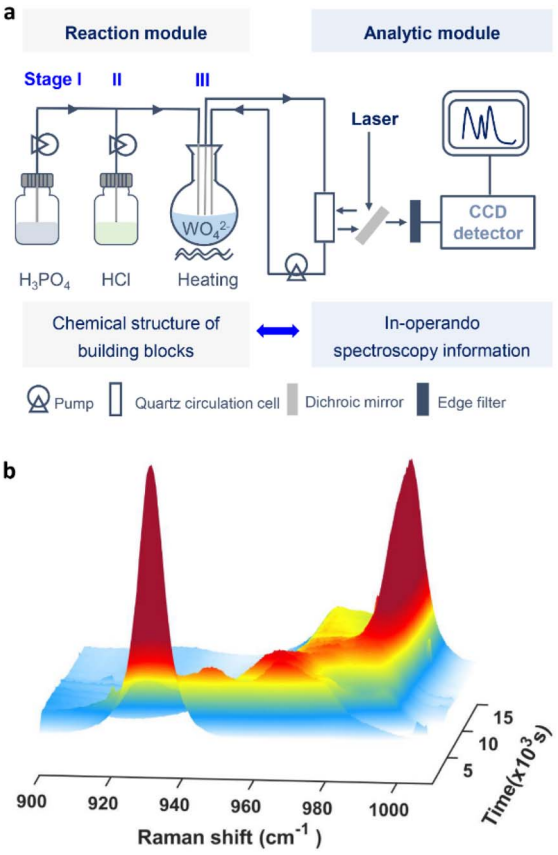

Fig. 1 (a) Schematic diagram of a visualization device for Wells–Dawson $\{P_2W_{18}\}$; (b) three-dimensional Raman waterfall mapping of the assembly process from WO_4^{2-} to $\{P_2W_{18}\}$.

stage II, sequential introduction of HCl (8.33 mL, flow rate 7.2 μL s^{-1}) to provide the acidity required for the subsequent reaction. In stage III, the heating and reflux procedure was performed according to the established method.[28] The analytical module incorporated *in operando* Raman spectroscopy was used for tracking building block evolution from monomer WO_4^{2-} to polynuclear $\{P_2W_{18}\}$.

Meanwhile, the whole reaction solution was circulated through a quartz flow cell at 100 rpm (16.15 mL min^{-1}), and the duration of stage I, stage II and stage III was over 15 000 seconds. The exposure time for each spectrum was 10 seconds. Thus, three-dimensional Raman mapping (Fig. 1b) was plotted based on more than 1300 Raman spectra. The signal intensity and spectral shifts with continuous variations were also accompanied by dynamic interconversion among intermediate species throughout the process. To realize precise establishment of reaction networks, the *in operando* Raman result was presented in the form of two-dimensional Raman mapping, wherein the identification of key intermediates was achieved through comparing with literature data and measuring the Raman shift and full width at half maximum (FWHM) of standard reference samples, followed by systematic validation of these assignments through ^{31}P NMR and ESI-MS.

Significantly, there were obvious Raman shifts during H_3PO_4 titration in stage I, as confirmed by the time-resolved two-dimensional Raman mapping spectra (Fig. 2 and S1). The dissociation of H_3PO_4 would provide anion templates (PO_4^{3-}) and protons, which functioned as structural templates for directing the building block assembly and protonation sources for inducing the aggregation of building blocks. The acidification by H_3PO_4 first induced the WO_4^{2-} (ν_s(W=O_d) at 931 cm^{-1}, Fig. S2) to aggregate into the iso-polyoxometalate building block $\{W_2\}$, as evidenced by the emergence of an intense new Raman band at 947 cm^{-1} and the *m*/*z* peaks of ESI-MS at 480.89 and 502.87 which were assigned to $[HW_2O_7]^-$ and $[NaW_2O_7]^-$, respectively (Fig. S3).[29,30] Meanwhile, part of the phosphoric acid existed as HPO_4^{2-}(Fig. 2 and S4). Subsequently, continuous H_3PO_4 addition until $n(H_3PO_4)/n(W)$ ratio = 0.5 would progressively lower solution pH from 9.16 to 8.05 (Fig. S5), and there was a new Raman shift appeared at 966 cm^{-1}. Based on the tungstate species reported in the literature that were stable within this pH range, and further supported by ^{31}P NMR analysis of reaction solution,[31] this species was identified as $\{PW_9\}$. Thus, the continuous addition of H_3PO_4 would drive the sequential transformations from WO_4^{2-} monomers and $\{W_2\}$ into $\{PW_9\}$ (Fig. 2, S3, S6 and S7). More interestingly, there was the appearance of a new distinct Raman band at 926 cm^{-1} corresponding to $\{P_2W_5\}$ (Fig. 2 and S8) when the ratio of $n(H_3PO_4)/n(W)$ ratio exceeded 0.5. This was further confirmed by the appearance of a peak at *m*/*z* values of 720.80 ($[P_2W_5O_{23}Na_4]^{2-}$) and 709.81 ($[P_2W_5O_{23}HNa_3]^{2-}$) in ESI-MS spectra (Fig. 2 and S9), as well as a new ^{31}P NMR signal peak at −1.75 ppm (Fig. 2 and S6). Actually, the further addition of H_3PO_4 decreased the pH of the solution down to 5.4 at $n(H_3PO_4)/n(W) = 1.1$. An almost complete conversion of $\{PW_9\}$ and $\{W_2\}$ into $\{P_2W_5\}$ was detected by the terminal phase of stage I, along with the emergence of $\{PW_{11}\}$ (Raman shift located at 964 cm^{-1} and 979 cm^{-1}, Fig. 2 and S10; ^{31}P NMR, Fig. 2 and S6).

A new Raman shift appeared at 968 cm^{-1}, which was consistently present during the titration of HCl in stage II. This was due to the existence of $[W_{12}O_{39}H_2Na_2]^{2-}$ (*m*/*z* = 1438.65) and $[W_{12}O_{39}HNa_3]^{2-}$ (*m*/*z* = 1449.64) as confirmed by ESI-MS (Fig. 2 and S11). From the end of stage I to the ratio of n(HCl)/n(W) approaching 0.6 in stage II (Fig. S12), the signal of the key intermediate building block $\{P_2W_5\}$ continuously weakened until it disappeared. Meanwhile, an enhancement of the $\{PW_{11}\}$ signal at 979 cm^{-1} and 964 cm^{-1} was observed, indicating that intermediate building blocks $\{P_2W_5\}$ restructured into intermediate units with high-nuclearity characteristics (Fig. 2, S6, S13 and S14). ESI-MS spectra also confirmed the existence of $\{PW_{11}\}$ based on *m*/*z* values of 1395.59 ($[PW_{11}O_{39}Na_5]^{2-}$) (Fig. 2 and S15). However, continued acidification protonated $\{PW_{11}\}$, inducing its partial conversion to $\{P_2W_{21}\}$, a process documented in previous studies.[31] The emergence of a new peak at 994 cm^{-1} was observed at the end of stage II, and the presence of $\{P_2W_{21}\}$ was further confirmed by ^{31}P NMR (−13.2 ppm, Fig. 2 and S13).[31]

Additionally, heating is also playing an important role in accelerating the building blocks transformation. As shown in the two-dimensional Raman mapping spectra during stage III of heating (Fig. 3a and S16), there was a gradual disappearance of peaks at 964 cm^{-1}, 979 cm^{-1}, 968 cm^{-1} and 994 cm^{-1}, accompanied by the emergence of new peaks at 992 cm^{-1} and 967 cm^{-1} when heated from room temperature to 60 °C. This indicated that the main intermediates protonated $\{PW_{11}\}$, iso-polyoxometalate $\{W_{12}\}$ and $\{P_2W_{21}\}$ interact with each other, involving the dynamic disassembly and reassembly of intermediate building blocks, ultimately converted into the thermodynamically stable product (Fig. 3a–c and S17). According to the Raman spectra of the standard sample $\{P_2W_{18}\}$ (Fig. S18 and S19), those Raman peaks exhibiting progressive intensity enhancement with prolonged thermal treatment were assigned to P–O stretching (992 cm^{-1}) and symmetrical stretching mode of W=O_d of $\{P_2W_{18}\}$ (967 cm^{-1}). Meanwhile, the solution changed from colourless to pale yellow. ESI-MS confirmed the existence of $\{P_2W_{18}\}$ with *m*/*z* = 872.69 $[P_2W_{18}O_{62}H]^{5-}$ (Fig. 3d and S20). ^{31}P NMR also found the generation of $\{P_2W_{18}\}$, which existed in two isomers, with α-$\{P_2W_{18}\}$ (−12.4 ppm) as the main product (Fig. S21).[31]

Actually, the structure evolution in stage III occurred spontaneously under ambient conditions, but typically required extended durations, as confirmed by the ^{31}P NMR investigation of the solution after 15 weeks of aging at the end of stage II (Fig. S22). Heating primarily enhanced the reaction kinetics in stage III by providing additional energy to facilitate the disassembly and reassembly of intermediate building blocks. Under heating, this interaction between $\{PW_{11}\}$ and iso-polyoxometalate $\{W_{12}\}$, together with the subsequent transformation into the $\{P_2W_{18}\}$ cluster, was expected to proceed rapidly. In our present studies, only the differences in intermediate species before and after heating were detectable.

As a result, through the application of precise reaction modules combined with *in operando* flow Raman techniques,

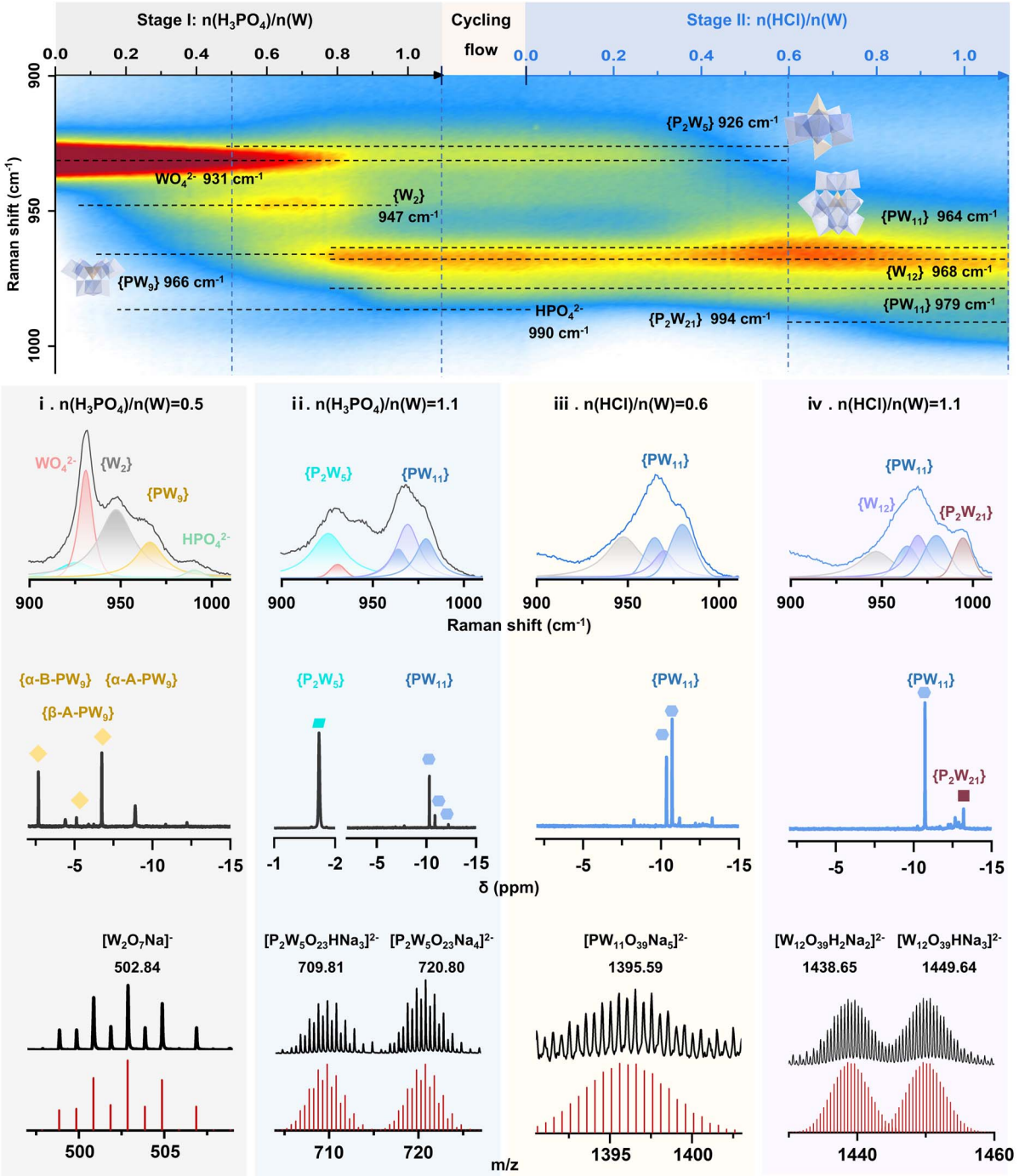

Fig. 2 Stage I–II of the acid titration process: the time-dependent 2D Raman mapping (900 cm^{-1} to 1010 cm^{-1}), along with corresponding Raman spectra, ^{31}P NMR spectra and ESI-MS spectra in the negative ion mode (the red and black lines represented simulated and experimental values, respectively) at different $n(H_3PO_4)/n(W)$ ratios or $n(HCl)/n(W)$ ratios. Stage I and stage II were separated by a cycling flow, which showed that the Raman signal remained unchanged during this interval.

ESI-MS and ^{31}P NMR, we systematically investigated the "bottom-up" assembly pathway from the monomers through several distinct main intermediates ($\{PW_9\}$, $\{P_2W_5\}$, and $\{PW_{11}\}$) to the final target product $\{P_2W_{18}\}$, as shown in Fig. 4. And developing more sensitive and advanced time-resolved characterization methods in the future will allow systematic investigation into the rapid disassembly and reassembly among the interactions of those building block intermediates.

Such *in operando* characterization will further facilitate the rational design of functional clusters *via* a direct "bottom-up" strategy based on those building blocks to realize different clusters with diversified applications. To validate the feasibility of the strategy, we chose key intermediate $\{PW_9\}$ as the primary

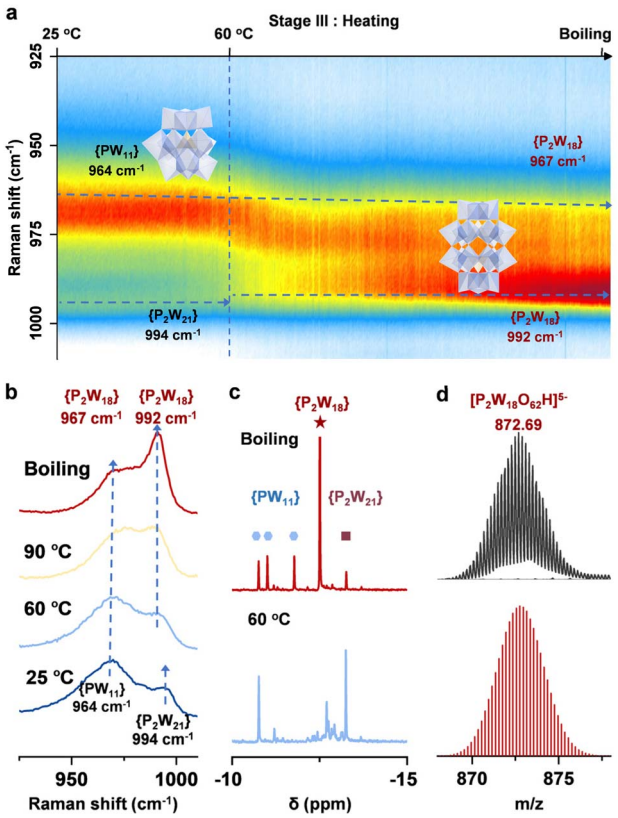

Fig. 3 (a) Stage III of heating: 2D Raman mapping (925 cm^{-1} to 1010 cm^{-1}); (b) the corresponding Raman spectra at different temperatures; (c) ^{31}P NMR spectrum of the reaction solution at 60 °C and on boiling; (d) ESI-MS spectrum in negative ion mode of the solution after 24-hour reflux (the red and black lines represented simulated and experimental values, respectively).

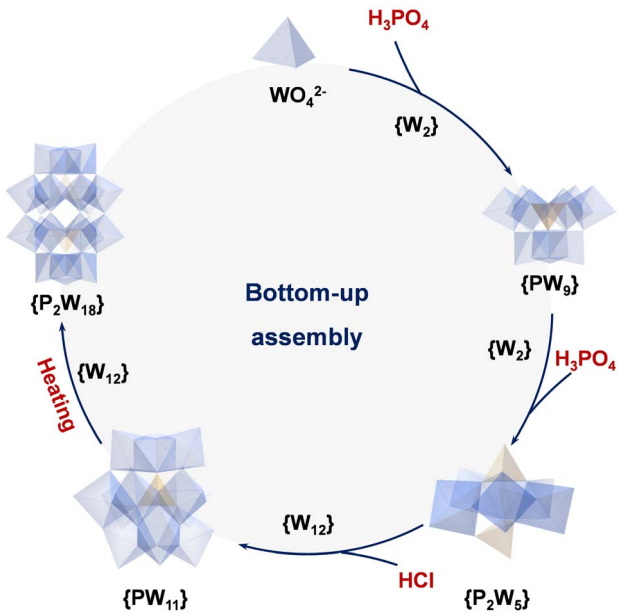

Fig. 4 Bottom-up assembly route from WO_4^{2-} to $\{P_2W_{18}\}$.

building unit to conduct the precise hierarchical reassembly. Specifically, based on the Raman results of stage I, the main intermediate $\{\alpha$-A-$PW_9\}$ was observed when the ratio of $n(H_3PO_4)/n(W)$ was 0.5 (Fig. S6), exhibiting a structure characterized by a tri-lacunary structure and C_{3v}-symmetry. By introducing K/Na–O polyhedra with Lewis acidity and flexible coordination numbers as structural linkers, highly negatively charged $PW_9O_{34}^{9-}$ structural units acting as the Lewis base served as SBUs for further oriented step-by-step reassembly.

Thus, $\{PW_9\}$ enabled the solution-phase hierarchical reassembly into architectures with interpenetrating three-dimensional channels of size 1.19 nm × 1.19 nm. The assembly of $\{PW_9\}$ units was directed by strong electrostatic interactions between Lewis acidic alkali metal cations (K^+ and Na^+) and the Lewis basic terminal and bridging oxo ligands of $\{PW_9\}$, with coordination interactions further stabilizing the architecture. As depicted in Fig. 5a, eight $\{PW_9\}$ SBUs acted as vertices to form a TBU with the octahedral K1–H_2O cage serving as the core of the structure (Fig. S23) while K2 and K3 stabilized the architecture by acting as a rigid shell (Fig. S24) and "structural rivet" (Fig. S25 and S26), respectively. Head-to-head linkage of $\{PW_9\}$ vertices through the Na/K–O polyhedron guided TBUs into a body-centered cubic arrangement, affording the extended framework as shown in Fig. 5a (more details are shown in Fig. S27, S28 and Tables S2–S4).

The intermediate building units played dual roles while constructing this framework structure. Beyond participating in hieratical assembly, $\{PW_9\}$ units acted as guest molecule templates in the void of the host framework. Instead of forming the densely packed structures typical of alkali metal systems because of the non-directional and long-range Coulomb forces characteristic of ionic bonds, this template-guided process yielded a 3D framework with nanopores. This empirically validated the template function of the negatively charged, nanoscale intermediate units in directing the hierarchical assembly. Ultimately, a novel host–guest architecture $\{[K_{66}Na_{14}H_{10}(H_2O)_{150}(PW_9O_{34})_8]\cdot(PW_9O_{34})_2\cdot 43H_2O\}$ (compound **1**, $\{PW_9\}_2@\{PW_9\}_8$) with three-dimensional interpenetrating channels accommodating discrete $\{PW_9\}$ was constructed. Its structure was determined by SCXRD, while elemental analysis by ICP-OES and thermogravimetric analysis (Fig. S29) confirmed the composition and consistency with the SCXRD-derived formula. Notably, the introduction of alkali metal ions enhanced the electronic shielding of the phosphorus atoms, resulting in an up-field shift in the ^{31}P NMR chemical shifts (−9.4 ppm, Fig. 5b).

Compared to single $\{PW_9\}$ existing randomly in solution, the high symmetry of compound **1** led to significant changes in the topological structure, as well as the electrochemical redox behaviours. As shown in Fig. 5c, giant cluster compound **1** under identical conditions manifested significantly enhanced redox activity, as evidenced by multiple distinct redox peaks at 0.23 V, 0.01 V, −0.49 V and −0.87 V *vs.* NHE, respectively. In particular, compound **1** exhibited a much higher peak current, reaching a peak current as high as 115 μA at −0.87 V whereas single $\{PW_9\}$ exhibited only a negligible reduction current of 9.5 μA at the same concentration. This suggests that the topological

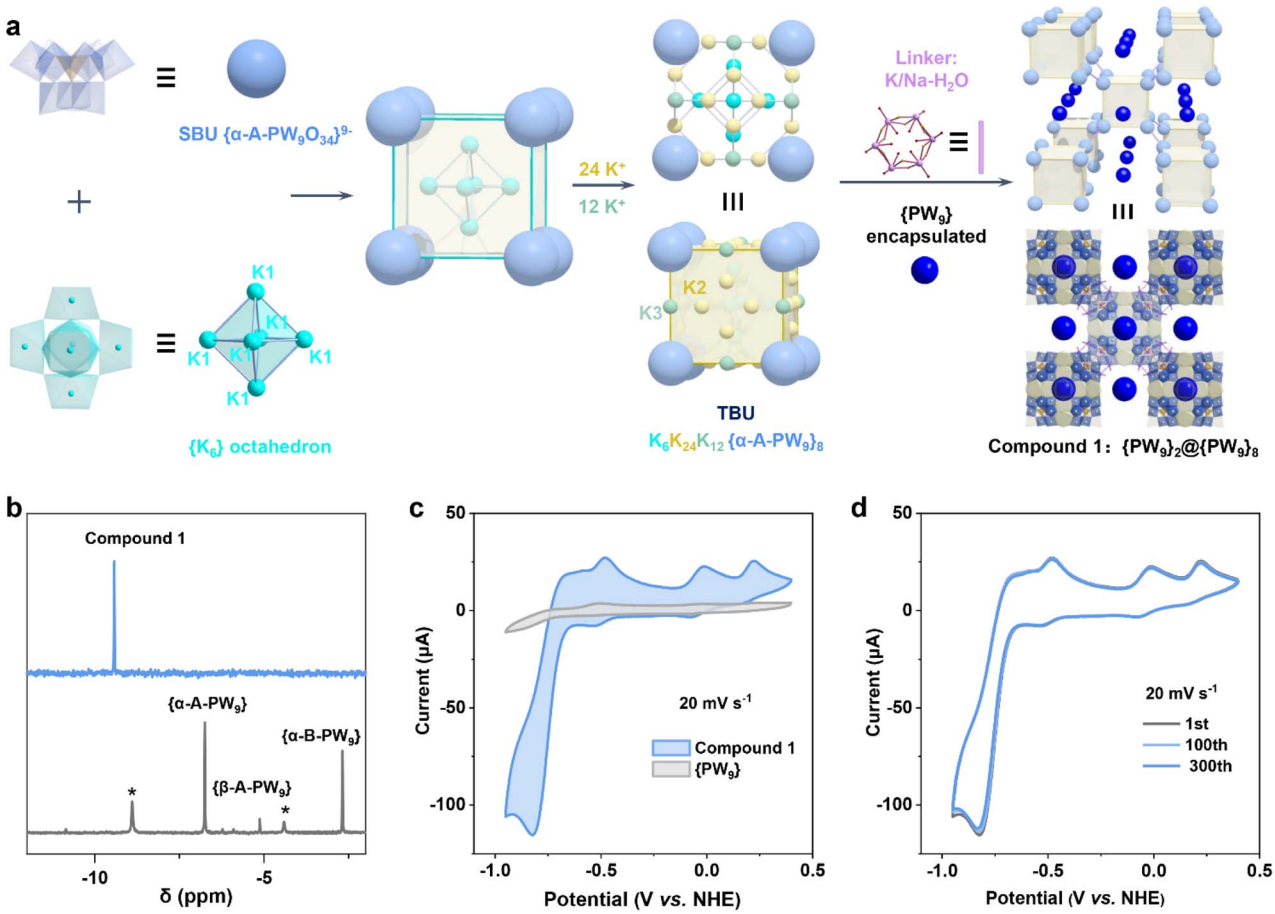

Fig. 5 Schematic overview of precise hierarchical reassembly, together with ^{31}P NMR and electrochemical property testing: (a) bottom-up hierarchical assembly from a single {PW_9} SBU into a {PW_9}$_8$ TBU and giant host–guest frameworks compound **1**; (b) ^{31}P NMR spectra: the gray line corresponded to the reaction solution when the ratio of $n(H_3PO_4)/n(W)$ was 0.5, while the blue line represented the aqueous solution of compound **1**; (c) cyclic voltammograms of 2.5 mM compound **1** and 2.5 mM {PW_9} at a scan rate of 20 mV s^{-1}, and (d) different numbers of cyclic voltammograms of compound **1** at a scan rate of 20 mV s^{-1}.

alteration may facilitate electron delocalization, manifesting in a more pronounced reduction process, as previously observed in earlier POM studies.[32–34] Consequently, conventional pairwise redox peaks were absent in the cyclic voltammogram of compound **1**. Instead, a reduction peak with a markedly high current appeared, consistent with the behaviour reported for giant polyoxometalates.[35] The stability of compound **1** (in both solution and solid states) was verified (Fig. S30 and S31), and multi-cycle cyclic voltammetry confirmed the electrochemical stability of the structure, as indicated by the near-complete overlap of the voltammograms from the 300th and first cycles at a scan rate of 20 mV s^{-1} (Fig. 5d). Furthermore, cyclic voltammetry at different scan rates (2 mV s^{-1} to 100 mV s^{-1}; Fig. S32) showed that potential of two oxidation peaks at positive potentials (nearly 0.01 V and 0.23 V) remained almost unchanged, indicating a relatively high degree of reversibility for these redox processes in compound **1**. The greater number of redox electrons, more negative potential, and relatively more reversible redox behaviour indicate its wider application prospects in electrochemistry. Specifically, its pronounced multi-electron redox behaviour serves as a key enabler for functionality in complex electrochemical systems that involve multiple electron transfers. The excellent topological structure of compound **1** underscored the key role of controllable flow synthesis in understanding the bottom-up assembly behaviour of POMs and precise hierarchical reassembly.

Conclusions

In summary, we established a flow chemistry synthesis platform integrated with *in operando* Raman spectroscopy for real-time monitoring of the dynamic evolution from monomer WO_4^{2-} to {P_2W_{18}} in solution. This approach enabled the explicit identification of key building blocks ({PW_9}, {P_2W_5}, and {PW_{11}}) and final products {P_2W_{18}} throughout the assembly process. Furthermore, leveraging the precision-guided bottom-up strategy, precision reassembly of solution-phase building blocks was achieved using intermediate {PW_9} as the SBU, yielding a giant cubic TBU (~1.9 nm) and further assembling a host–guest architecture of compound **1** with three-dimensional interpenetrating channels accommodating discrete {PW_9}. Unlike individual building units {PW_9} that exhibited only a minimal reduction peak, giant clusters of compound **1** formed through bottom-up reassembly and demonstrated

multiple redox peaks accompanied by a pronounced enhancement in peak current. This observation highlighted how precision reassembly strategies optimized structural unit functionality (*e.g.*, electrochemical redox behaviour), and the developed methodology—combining dynamic monitoring, quantitative profiling, and precision manipulation—not only deciphered the hierarchical assembly mechanism of the clusters but also established a new paradigm for the controllable synthesis of polyoxometalates and functional cluster materials.

Author contributions

J. C. proposed the project. J. C. and K. Z. wrote the manuscript. K. Z. carried out all the experiments. K. L. helped with Raman analysis and the analysis of the crystallographic structure. L. F. helped with the analysis of nuclear magnetic data. L. Y. provided assistance in completing revisions to this manuscript.

Conflicts of interest

There are no conflicts to declare.

Data availability

CCDC 2470529 contains the supplementary crystallographic data for this paper.[36]

Further details of the crystal structure determination can be obtained from the Fachinformationszentrum Karlsruhe, D-76344 Eggenstein-Leopoldshafen (Germany) according to the depository numbers CSD 2470529 for compound **1**.

Supplementary information (SI): all supporting data for this article, including materials and methods, characterization data (Raman, NMR, ESI-MS, SCXRD, TGA, PXRD, ICP-OES), solution pH, and CV measurements have been included as SI. See DOI: **https://doi.org/10.1039/d5sc07121f**.

Acknowledgements

We acknowledge financial support from the National Natural Science Foundation of China (NSFC, 22441030, 22393901, 22021001, and 22272143), the National Key Research and Development Program (2021YFA1502300), the Fundamental Research Funds for the Central Universities (20720250005), and the Fujian Provincial Natural Science Foundation of China (2024J01213135). Dr Ke Li is also thankful for the support of a fellowship of the China Postdoctoral Science Foundation (2024M761765).

Notes and references

1 B. Rausch, M. D. Symes, G. Chisholm and L. Cronin, Decoupled catalytic hydrogen evolution from a molecular metal oxide redox mediator in water splitting, *Science*, 2014, **345**, 1326–1330.

2 M. Martin-Sabi, J. Soriano-López, R. S. Winter, J.-J. Chen, L. Vilà-Nadal, D.-L. Long, J. R. Galán-Mascarós and L. Cronin, Redox tuning the Weakley-type polyoxometalate archetype for the oxygen evolution reaction, *Nat. Catal.*, 2018, **1**, 208–213.

3 K. S. Westendorff, M. J. Hülsey, T. S. Wesley, Y. Román-Leshkov and Y. Surendranath, Electrically driven proton transfer promotes Brønsted acid catalysis by orders of magnitude, *Science*, 2024, **383**, 757–763.

4 I. A. Weinstock, R. E. Schreiber and R. Neumann, Dioxygen in Polyoxometalate Mediated Reactions, *Chem. Rev.*, 2017, **118**, 2680–2717.

5 S. Amthor, S. Knoll, M. Heiland, L. Zedler, C. Li, D. Nauroozi, W. Tobaschus, A. K. Mengele, M. Anjass, U. S. Schubert, B. Dietzek-Ivanšić, S. Rau and C. Streb, A photosensitizer–polyoxometalate dyad that enables the decoupling of light and dark reactions for delayed on-demand solar hydrogen production, *Nat. Chem.*, 2022, **14**, 321–327.

6 D. H. Li, X. Y. Zhang, J. Q. Lv, P. W. Cai, Y. Q. Sun, C. Sun and S. T. Zheng, Photo-Activating Biomimetic Polyoxomolybdate for Boosting Oxygen Evolution in Neutral Electrolytes, *Angew. Chem., Int. Ed.*, 2023, **62**, e202312706.

7 J.-J. Chen, M. D. Symes and L. Cronin, Highly reduced and protonated aqueous solutions of [P2W18O62]6− for on-demand hydrogen generation and energy storage, *Nat. Chem.*, 2018, **10**, 1042–1047.

8 F. Ai, Z. Wang, N.-C. Lai, Q. Zou, Z. Liang and Y.-C. Lu, Heteropoly acid negolytes for high-power-density aqueous redox flow batteries at low temperatures, *Nat. Energy*, 2022, **7**, 417–426.

9 L. Yang, Y. Hao, J. Lin, K. Li, S. Luo, J. Lei, Y. Han, R. Yuan, G. Liu, B. Ren and J. Chen, POM Anolyte for All-Anion Redox Flow Batteries with High Capacity Retention and Coulombic Efficiency at Mild pH, *Adv. Mater.*, 2022, **34**, 2107425.

10 L. Yang, S. Zhang, K. Li, H. Wu, T. Wu, D. Wu and J. Chen, Tuning the inner- and outer-sphere electron transfer behavior of aqueous {CoW12} polyoxometalate clusters for redox flow batteries exceeding 1.5V, *Energy Storage Mater.*, 2024, **65**, 103149.

11 A. Magerat, S. Hermans and E. M. Gaigneaux, A novel versatile platform as efficient deoxydehydration (DODH) catalysts: Keggin polyoxometalates, *Appl. Catal. B Environ.*, 2025, **375**, 125432.

12 E. Arendt, S. Ghislain and E. M. Gaigneaux, Operando investigation of the catalytic behavior of Wells–Dawson heteropolycompounds in the oxidation of propene, *Catal. Today*, 2010, **155**, 227–240.

13 J. M. Clemente-Juan, E. Coronado and A. Gaita-Ariño, Magnetic polyoxometalates: from molecular magnetism to molecular spintronics and quantum computing, *Chem. Soc. Rev.*, 2012, **41**, 7464–7478.

14 M. A. AlDamen, J. M. Clemente-Juan, E. Coronado, C. Martí-Gastaldo and A. Gaita-Ariño, Mononuclear Lanthanide Single-Molecule Magnets Based on Polyoxometalates, *J. Am. Chem. Soc.*, 2008, **130**, 8874–8875.

15 D.-L. Long, E. Burkholder and L. Cronin, Polyoxometalate clusters, nanostructures and materials: From self assembly to designer materials and devices, *Chem. Soc. Rev.*, 2007, **36**, 105–121.

16 X. K. Lian, H. B. Chen, Y. D. Lin, X. X. Li and S. T. Zheng, Polyoxometalate-based all-inorganic open frameworks, *Coord. Chem. Rev.*, 2023, **497**, 215440.
17 Y. F. Song and R. Tsunashima, Recent advances on polyoxometalate-based molecular and composite materials, *Chem. Soc. Rev.*, 2012, **41**, 7384–7402.
18 Z. Li, L. D. Lin, H. Yu, X. X. Li and S. T. Zheng, All-Inorganic Ionic Porous Material Based on Giant Spherical Polyoxometalates Containing Core-Shell K(6) @K(36) -Water Cage, *Angew. Chem., Int. Ed.*, 2018, **57**, 15777–15781.
19 L. Yang, J. Lei, J. M. Fan, R. M. Yuan, M. S. Zheng, J. J. Chen and Q. F. Dong, The Intrinsic Charge Carrier Behaviors and Applications of Polyoxometalate Clusters Based Materials, *Adv. Mater.*, 2021, **33**, 2005019.
20 K. Li, S. Zhang, K. L. Zhu, L. P. Cui, L. Yang and J. J. Chen, Revealing the Electrocatalytic Self-Assembly Route from Building Blocks into Giant Mo-Blue Clusters, *J. Am. Chem. Soc.*, 2023, **145**, 24889–24896.
21 C. Busche, L. Vilà-Nadal, J. Yan, H. N. Miras, D.-L. Long, V. P. Georgiev, A. Asenov, R. H. Pedersen, N. Gadegaard, M. M. Mirza, D. J. Paul, J. M. Poblet and L. Cronin, Design and fabrication of memory devices based on nanoscale polyoxometalate clusters, *Nature*, 2014, **515**, 545–549.
22 P. X. Wu, Z. W. Guo, R. D. Lai, X. X. Li, C. Sun and S. T. Zheng, Giant Polyoxoniobate-Based Inorganic Molecular Tweezers: Metal Recognitions, Ion-Exchange Interactions and Mechanism Studies, *Angew. Chem., Int. Ed.*, 2023, **62**, e202217926.
23 P. Yin, B. Wu, E. Mamontov, L. L. Daemen, Y. Cheng, T. Li, S. Seifert, K. Hong, P. V. Bonnesen, J. K. Keum and A. J. Ramirez-Cuesta, X-ray and Neutron Scattering Study of the Formation of Core–Shell-Type Polyoxometalates, *J. Am. Chem. Soc.*, 2016, **138**, 2638–2643.
24 Z. Wang, H. F. Su, Y. Z. Tan, S. Schein, S. C. Lin, W. Liu, S. A. Wang, W. G. Wang, C. H. Tung, D. Sun and L. S. Zheng, Assembly of silver Trigons into a buckyball-like Ag(180) nanocage, *Proc. Natl. Acad. Sci. U.S.A.*, 2017, **114**, 12132–12137.
25 Y. K. Deng, H. F. Su, J. H. Xu, W. G. Wang, M. Kurmoo, S. C. Lin, Y. Z. Tan, J. Jia, D. Sun and L. S. Zheng, Hierarchical Assembly of a Mn(II)15Mn(III)4 Brucite Disc: Step-by-Step Formation and Ferrimagnetism, *J. Am. Chem. Soc.*, 2016, **138**, 1328–1334.
26 J. M. Cameron, L. Vilà-Nadal, R. S. Winter, F. Iijima, J. C. Murillo, A. Rodríguez-Fortea, H. Oshio, J. M. Poblet and L. Cronin, Investigating the Transformations of Polyoxoanions Using Mass Spectrometry and Molecular Dynamics, *J. Am. Chem. Soc.*, 2016, **138**, 8765–8773.
27 H. N. Miras, G. J. T. Cooper, D.-L. Long, H. Bögge, A. Müller, C. Streb and L. Cronin, Unveiling the Transient Template in the Self-Assembly of a Molecular Oxide Nanowheel, *Science*, 2010, **327**, 72–74.
28 C. R. Graham and R. G. Finke, The Classic Wells−Dawson Polyoxometalate, K6[α-P2W18O62]·14H2O. Answering an 88 Year-Old Question: What Is Its Preferred, Optimum Synthesis?, *Inorg. Chem.*, 2008, **47**, 3679–3686.
29 N. Weinstock, H. Schulze and A. Müller, Assignment of ν2 (E) and ν4 (F2) of tetrahedral species by the calculation of the relative Raman intensities: The vibrational spectra of VO43−, CrO42−, MoO42−, WO42−, MnO4−, TcO4−, ReO4−, RuO4, and OsO4, *J. Chem. Phys.*, 1973, **59**, 5063–5067.
30 J. Wang, J. L. You, A. A. Sobol, L. M. Lu, M. Wang, J. Wu, X. M. Lv and S. M. Wan, In-situhigh temperature Raman spectroscopic study on the structural evolution of Na2W2O7from the crystalline to molten states, *J. Raman Spectrosc.*, 2017, **48**, 298–304.
31 R. I. Maksimovskaya and G. M. Maksimov, 31P NMR studies of hydrolytic conversions of 12-tungstophosphoric heteropolyacid, *Coord. Chem. Rev.*, 2019, **385**, 81–99.
32 J. J. Chen, L. Vila-Nadal, A. Sole-Daura, G. Chisholm, T. Minato, C. Busche, T. Zhao, B. Kandasamy, A. Y. Ganin, R. M. Smith, I. Colliard, J. J. Carbo, J. M. Poblet, M. Nyman and L. Cronin, Effective Storage of Electrons in Water by the Formation of Highly Reduced Polyoxometalate Clusters, *J. Am. Chem. Soc.*, 2022, **144**, 8951–8960.
33 Z. Li, Z. Zhang, H. Hu, Q. Liu and X. Wang, Synthesis of two-dimensional polyoxoniobate-based clusterphenes with in-plane electron delocalization, *Nat. Synth.*, 2023, **2**, 989–997.
34 H. Li, L. Zheng, Q. Lu, Z. Li and X. Wang, A monolayer crystalline covalent network of polyoxometalate clusters, *Sci. Adv.*, 2023, **9**, eadi6595.
35 T. Zhao, N. L. Bell, G. Chisholm, B. Kandasamy, D. L. Long and L. Cronin, Aqueous solutions of super reduced polyoxotungstates as electron storage systems, *Energy Environ. Sci.*, 2023, **16**, 2603–2610.
36 CCDC 2470529: Experimental Crystal Structure Determination, 2025, DOI: **10.25505/fiz.icsd.cc2nxshw**.